HHS Public Access

Author manuscript

Med Image Anal. Author manuscript; available in PMC 2016 October 01.

Published in final edited form as:

Med Image Anal. 2015 October ; 25(1): 72–85. doi:10.1016/j.media.2015.04.002.

Tumor Growth Prediction with Reaction-Diffusion and Hyperelastic Biomechanical Model by Physiological Data Fusion

Ken C. L. Wong[a], **Ronald M. Summers**[a], **Electron Kebebew**[b], and **Jianhua Yao**[a,*]

[a]Clinical Image Processing Service, Radiology and Imaging Sciences, Clinical Center, NIH, Bethesda, MD, USA

[b]Endocrine Oncology Branch, National Cancer Institute, NIH, Bethesda, MD, USA

Abstract

The goal of tumor growth prediction is to model the tumor growth process, which can be achieved by physiological modeling and model personalization from clinical measurements. Although image-driven frameworks have been proposed with promising results, several issues such as infinitesimal strain assumptions, complicated personalization procedures, and the lack of functional information, may limit their prediction accuracy. In view of these issues, we propose a framework for pancreatic neuroendocrine tumor growth prediction, which comprises a FEM-based tumor growth model with coupled reaction-diffusion equation and nonlinear biomechanics. Physiological data fusion of structural and functional images is used to improve the subject-specificity of model personalization, and a derivative-free global optimization algorithm is adopted to facilitate the complicated model and accommodate flexible choices of objective functions. With this flexibility, we propose an objective function accounting for both the tumor volume difference and the root-mean-squared error of intracellular volume fractions. Experiments were performed on synthetic and clinical data to verify the parameter estimation capability and the prediction performance. Comparisons of using different biomechanical models and objective functions were also performed. From the experimental results of eight patient data sets, the average recall, precision, Dice coefficient, and relative volume difference between predicted and measured tumor volumes were 84.5±6.9%, 85.8±8.2%, 84.6±1.7%, and 14.2±8.4%, respectively.

Keywords

Tumor growth prediction; model personalization; physiological data fusion; nonlinear solid mechanics; derivative-free optimization

*Corresponding author. ken.wong@nih.gov (Ken C. L. Wong), rsummers@cc.nih.gov (Ronald M. Summers), kebebewe@mail.nih.gov (Electron Kebebew), jyao@cc.nih.gov (Jianhua Yao).

1. Introduction

The goal of tumor growth prediction is to accurately model the tumor growth process, which is mainly achieved by physiological modeling and model personalization from clinical measurements. If accurate prediction can be achieved from noninvasive measurements, better treatment planning and patient prioritization can be determined, allowing more efficient use of resources. For example, if tumor doubling times of pancreatic neuroendocrine tumors can be estimated, the risk of metastatic disease, operative resection, and unnecessary testing can be better managed (Blansfield et al., 2007). Furthermore, if phenotype or genotype information can be revealed from the personalized growth model, outcomes of drug treatments can be improved with reduced toxicity (Clayton et al., 2006; Schilsky, 2010).

Tumor growth modeling is particularly pertinent for tumors that are either unresectable, or that are not removed until they reach a certain size threshold (Kazanjian et al., 2006; Ehehalt et al., 2009). Therefore, image-based tumor growth modeling has been actively researched. Image-based tumor growth personalization requires three key components: a tumor growth model, medical images, and a parameter estimation algorithm. The tumor growth model accounts for the general physiological properties derived from ex vivo or in vitro experiments, or in vivo animal tests, providing a powerful tool for tumor growth prediction. On the other hand, medical images provide the in vivo measurements of the patient, revealing the structural or functional information of the underlying physiological status. Through computational or mathematical algorithms, the complementary information from the model and images can be combined together to provide patient-specific tumor growth prediction.

Tumor growth is the abnormal growth of tissue, which usually involves cell invasion and mass effect (Friedl et al., 2012). In collective cell invasion, tumor cells migrate as a cohesive and multicellular group with retained cell-cell junctions and penetrate to the surrounding normal tissues. Mass effect is caused by expansive growth, for which the increase in tumor volume leads to multicellular outward pushing with intact cell-cell junctions, and tumor cells may be displaced by the volume expansion and pushing. If coupled with migration, mass effect contributes to and enhances collective invasion. To model invasion and mass effect, most image-based frameworks use macroscopic models to trade-off between realism and computationally efficiency. Cell invasion has mostly been modeled through reaction-diffusion equations which describe cell migrations and proliferations (Clatz et al., 2005; Hogea et al., 2008; Konukoglu et al., 2010; Menze et al., 2011; Chen et al., 2013; Liu et al., 2014). Cell migrations have been modeled as diffusion of cell densities, which can be anisotropic or inhomogeneous when the corresponding tissue structure information is available (Clatz et al., 2005; Hogea et al., 2008; Konukoglu et al., 2010; Menze et al., 2011). Cell proliferations have been modeled as the increase of local cell densities, which can be described by the logistic function (Hogea et al., 2008; Konukoglu et al., 2010; Menze et al., 2011; Liu et al., 2014) or the Gompertz function (Clatz et al., 2005; Chen et al., 2013). Mass effect has usually been modeled using biomechanics. Although nonlinear mechanics should be used for soft tissue modeling (Fung, 1993) and is the mainstream in the tissue growth modeling society (Menzel and Kuhl, 2012), for simplicity, most image-based tumor growth

modeling frameworks use the less realistic linear stress-strain relation with infinitesimal strain assumption (Clatz et al., 2005; Hogea et al., 2008; Chen et al., 2013; Liu et al., 2014) with few exceptions (Kyriacou et al., 1999). Different approaches have been used to incorporate the mechanical models, such as using the traditional solid mechanics approaches with finite element methods (FEM) (Clatz et al., 2005; Chen et al., 2013), or approximating the mechanical effects as an extra advection term in the reaction-diffusion equation (Hogea et al., 2008; Liu et al., 2014).

For subject-specific tumor growth prediction, different personalization frameworks have been proposed to incorporate different image modalities to personalize different tumor growth models. In Hogea et al. (2008), a reaction-advection-diffusion equation describing both the invasion and mass effect of brain gliomas growth was solved using a fictitious domain method. Using a Lagrangian functional with manually identified landmarks from brain magnetic resonance images (MRI) as measurements, the model was personalized using adjoint-based partial-differential-equation-constrained (PDE-constrained) optimization. In Konukoglu et al. (2010), a reaction-diffusion-based brain gliomas growth model was personalized using structural information from MRI and diffusion tensor images. The evolution of the tumor delineation was approximated by a modified anisotropic eikonal model, which could be efficiently solved by a recursive anisotropic fast marching approach. By fixing the proliferation rates, the diffusion coefficients were estimated by comparing between the simulated and measured tumor delineations using the UOBYQA (Unconstrained Optimization BY Quadratic Approximation) optimization algorithm. In Chen et al. (2013), kidney tumor growth was modeled by a coupled reaction-diffusion and linear mechanical model, which was solved using FEM. Using the segmented tumor volumes from contrast-enhanced computed tomographic (CT) images at multiple time points, the model parameters were estimated by the hybrid optimization parallel search package (HOPSPACK). The estimated proliferation rates at different time points were combined together by exponential curve fitting to obtain the proliferation rate at the current time point for the growth prediction. In Liu et al. (2014), using a similar model and optimization approach in Hogea et al. (2008), a multimodal framework was proposed for pancreatic tumor growth prediction. With the intracellular volume fractions (ICVF) obtained from contrast-enhanced CT images, and the standardized uptake values (SUV) obtained from 2-[^{18}F]-fluoro-2-deoxy-D-glucose positron emission tomography (FDG-PET), the model was personalized with fused functional and structural information.

Although these frameworks are promising, several issues may limit their prediction performances. For simplicity, most frameworks use linear stress-strain relation with infinitesimal strain assumption. In continuum mechanics, linear strain-displacement approximation should only be used when deformation is less than 5% (Bathe, 1996; Holzapfel, 2000), which is usually not the case for tumor growth. Furthermore, most biological tissues should be modeled as hyper-viscoelastic materials (Fung, 1993). For parameter estimation, Hogea et al. (2008) and Liu et al. (2014) formulated the problem as adjoint-based PDE-constrained optimization, whose formulations are very complicated and the analytical derivatives of the model and objective function are required. Such an approach is not suitable for more complex models, and may limit the choices of more realistic models and better objective functions. Moreover, except Liu et al. (2014), only structural but not

functional information was utilized, which may limit the patient-specificity of the personalized model and thus its prediction capability.

In view of these issues, we propose here a framework for pancreatic neuroendocrine tumor growth prediction (Figure 1). Pancreatic neuroendocrine tumors are abnormal growths of hormone-producing cells in the pancreas (Ries et al., 2007; Ehehalt et al., 2009). They are very rare, with only about 1,000 new cases in the United States per year. They are also slow growing, and usually not treated until reaching a certain size threshold. Our framework includes:

- A FEM-based tumor growth model with coupled reaction-diffusion equation and hyperelastic biomechanical model to improve physiological plausibility.
- A derivative-free global optimization algorithm for model parameter estimation to facilitate the complicated model and accommodate flexible choices of the objective function.
- Physiological data fusion of contrast-enhanced CT and FDG-PET images to improve subject-specificity.

Using this framework, more complicated objective functions can be studied, and we propose an objective function which accounts for both the volume difference and the root-mean-squared error of ICVF between simulations and measurements. Sensitivity analysis was performed to understand the impacts of different model parameters. Experiments were performed on synthetic data to verify the parameter estimation capability of the framework under different growth rates, and on clinical data for the prediction performance in reality. Comparisons of using different biomechanical models and objective functions are also presented.

Although this work is partially based on the work of Liu et al. (2014) in terms of computing ICVF from contrast-enhanced CT images and computing proliferation rates from FDG-PET images, there are fundamental differences between these two works:

i. **Biomechanical model**. In this paper, a hyperelastic biomechanical model is used instead of a linear model. Furthermore, in Liu et al. (2014), the mechanical response was approximated as advection in a reaction-advection-diffusion equation solved by the finite difference method, which is simple but physically less accurate. In contrast, in this paper, the total-Lagrangian formulation is used with FEM for more accurate mechanical response but increased computational complexity.

ii. **Objective function**. In Liu et al. (2014), only the ICVF differences between the simulations and measurements were used. In this paper, apart from the ICVF differences, the differences between the simulated and segmented tumor volumes are also considered.

iii. **Optimization method**. In Liu et al. (2014), the adjoint-based PDE-constrained optimization was used to estimate the model parameters, which requires the analytical derivatives of the objective function and model. In this paper, as the objective function and model are more complicated, it is difficult to derive the

analytical derivatives and thus a more flexible gradient-free optimization method is used.

In this paper, the macroscopic tumor growth model is described in Section 2, followed by the image-derived information in Section 3, and the model personalization in Section 4. Results of the sensitivity analysis are presented in Section 5, and the experimental results on synthetic and clinical data are presented in Section 6. The discussion is provided in Section 7.

2. Macroscopic Tumor Growth Model

The tumor growth model comprises morphological and physiological knowledge obtained from ex vivo or in vitro experiments, providing a powerful prediction tool. With the consideration of the physiological plausibility of the model, the computational complexity of the inverse problem, and the resolution and nature of the radiological images (CT and PET), a macroscopic tumor growth model is proposed.

2.1. Reaction-Diffusion Equation for Proliferation and Invasion

Tumor proliferation is the creation of tumor cells, and tumor invasion is the penetration of tumor cells to the surrounding tissues (Friedl et al., 2012; Kam et al., 2012). To simulate these processes, different cell-based, macroscopic, multiscale, continuum, and discrete models have been proposed with different physiological plausibility and computational complexity (Alarcón et al., 2003; Jiang et al., 2005; Byrne, 2010; Kam et al., 2012). Although cell-based and multiscale models can better account for subcellular physiology, these complicated models can be difficult to personalize using medical images because of the numbers and natures of the parameters. For discrete models such as those using cellular automata, although some are feasible for large-scale simulations, their discrete nature may limit the flexibility of choosing the objective function for model personalization. Therefore, to facilitate the complicated inverse problem of model personalization from images, the macroscopic reaction-diffusion equation is usually used (Hogea et al., 2008; Konukoglu et al., 2010; Chen et al., 2013; Liu et al., 2014).

Consider a reaction-diffusion equation with logistic growth:

$$\frac{\partial N}{\partial t} = \mathrm{div}(\mathbf{D}\nabla N) + \rho N\left(1 - \frac{N}{K}\right) \quad (1)$$

with the first term for tumor invasion and the second term for logistic cell proliferation. N is the number of tumor cells and K is the carrying capacity. $\mathbf{D}$ is the anisotropic diffusion tensor characterizing the invasive property, which is a diagonal matrix with components D_x, D_y, and D_z regardless of the tissue structure. Directional diffusion can be included by incorporating the tissue structure, but it is not considered as diffusion tensor images are unavailable in our data sets, though orthotropic diffusion is used to account for possible anisotropic invasion. ρ is the proliferation rate, which can be computed from FDG-PET images for better subject-specificity (see Section 3.2). Dividing both sides of (1) by K, we have:

$$\frac{\partial \theta}{\partial t} = \mathrm{div}(\mathbf{D}\nabla\theta) + \rho\theta(1-\theta) \quad (2)$$

where $\theta = (N/K) \in [0, 1]$ represents the normalized tumor cell ratio. As the number of cells is proportional to the space they occupy, we represent θ by ICVF, which is the local ratio of the intracellular space to the tissue volume. ICVF can be computed from contrast-enhanced CT images to provide the initial conditions of (2) (see Section 3.1), and can be used as the measurements for model personalization. In our implementation, (2) is reformulated into the Galerkin weak form and solved using FEM (Rogers and McCulloch, 1994; Bathe, 1996).

As (2) directly connects ICVF and proliferation rate derived from the images, it plays an important role of physiological data fusion. Although this equation is relatively simple, its capability of simulating realistic macroscopic tumor growth has been well-verified (Gatenby and Gawlinski, 1996; Clatz et al., 2005; Byrne, 2010).

2.2. Hyperelastic Mechanical Model for Mass Effect

Mass effect is the growing tumor mass pushing and displacing the surrounding tissues (Friedl et al., 2012). Although nonlinear mechanical models have been proposed to account for mass effect (Ambrosi and Mollica, 2002; Graziano and Preziosi, 2007), for simplicity, most image-based model personalization frameworks use linear mechanical models (Hogea et al., 2008; Chen et al., 2013; Liu et al., 2014) with few exceptions (Kyriacou et al., 1999). Nevertheless, infinitesimal strain assumption should only be made for small deformation (< 5%) (Bathe, 1996; Holzapfel, 2000), which is usually not the case for biological tissues (Fung, 1993). Furthermore, non-linear constitutive law is required for enforcing tissue incompressibility in large deformation (Holzapfel, 2000). Therefore, for better physiological plausibility, we use the modified Saint-Venant-Kirchhoff constitutive law to model the tissue as nearly incompressible and isotropic material (Holzapfel, 2000):

$$\psi(\boldsymbol{\varepsilon}) = \frac{1}{2}\lambda(J-1)^2 + \mu\mathrm{Tr}(\bar{\boldsymbol{\varepsilon}}^2) \quad (3)$$

where $J = \det \mathbf{F}$, with $\mathbf{F}$ the deformation gradient tensor, and $J = 1$ for isovolumetric deformation. $\bar{\boldsymbol{\varepsilon}} = \frac{1}{2}(\bar{\mathbf{F}}^{\mathrm{T}}\bar{\mathbf{F}} - \mathbf{I})$ is the isovolumetric part of the Green-Lagrange strain tensor $\boldsymbol{\varepsilon} = \frac{1}{2}(\mathbf{F}^{\mathrm{T}}\mathbf{F} - \mathbf{I})$. $\bar{\mathbf{F}} = J^{-\frac{1}{3}}\mathbf{F}$ and thus $\det \bar{\mathbf{F}} \equiv 1$. The first and the second term of (3) account for the volumetric and isochoric elastic response, respectively, and thus λ is the bulk modulus and μ is the shear modulus. In our model, the tumor and its surrounding tissues have different mechanical parameters. The second-order second Piola-Kirchhoff (PKII) stress tensor ($\partial\psi/\partial\boldsymbol{\varepsilon}$) and the fourth-order elasticity tensor ($\partial^2\psi/\partial\boldsymbol{\varepsilon}^2$) can be derived from (3) to provide the nonlinear stress-strain relation.

To simulate mass effect, we compute the pushing force from the ICVF (θ) as (Clatz et al., 2005):

$$\mathbf{f}_b = -\gamma\nabla\theta \quad (4)$$

where γ is the force scaling parameter. Therefore, the tumor pushes towards the directions with lower tumor cell densities. As the deformation rate is slow for tumor growth, the pushing force ($\mathbf{f}_b$) is related to the Cauchy stress tensor ($\boldsymbol{\sigma}$) using the static equilibrium equation:

$$\mathrm{div}(\boldsymbol{\sigma})+\mathbf{f}_b=0 \quad (5)$$

From (5), the total-Lagrangian formulation can be derived and the Cauchy stress tensor is transformed into the PKII stress tensor (Bathe, 1996). With the stress-strain relation provided by the elasticity tensor derived from (3), the biomechanical model is complete and can be solved using FEM (Bathe, 1996). The Newton-Raphson method is used with incremental decomposition to ensure the accuracy of the nonlinear solution (Bathe, 1996). Different passive mechanical parameters λ and μ are assigned to the tumor and its surrounding normal tissues.

Apart from the hyperelastic mechanical model, we also performed experiments on a linear mechanical model for comparison. The linear stress-strain relation of the model is described by the Hooke's law (Bathe, 1996):

$$\boldsymbol{\sigma}=\mathbb{C}_{\varepsilon} \quad (6)$$

where $\mathbb{C}$ is an isotropic elasticity tensor characterized by the Young's modulus (E) and Poisson's ratio (ν). Its matrix representation is given as:

$$[\mathbb{C}]=\frac{E}{(1+\nu)(1-2\nu)}\begin{bmatrix} 1-\nu & \nu & \nu & 0 & 0 & 0 \\ \nu & 1-\nu & \nu & 0 & 0 & 0 \\ \nu & \nu & 1-\nu & 0 & 0 & 0 \\ 0 & 0 & 0 & \frac{1-2\nu}{2} & 0 & 0 \\ 0 & 0 & 0 & 0 & \frac{1-2\nu}{2} & 0 \\ 0 & 0 & 0 & 0 & 0 & \frac{1-2\nu}{2} \end{bmatrix} \quad (7)$$

As infinitesimal strain assumption is also used, the mechanical model is linear and the Newton-Raphson method is not required.

3. Image-Derived Information

Image-derived information is necessary for patient-specific tumor growth prediction. As tumor growth involves morphological and physiological functions (Friedl et al., 2012), both structural and functional images are adopted in our framework to improve the patient-specificity and physiological plausibility of the personalized model.

3.1. ICVF from Contrast-Enhanced CT Images

As the number of cells is proportional to the intracellular space they occupy, we represent the normalized tumor cell ratio (θ) in (2) by ICVF, which is the local ratio of the intracellular space to the tissue volume that can be computed from contrast-enhanced CT images. The concept and formulation of ICVF are based on the computation of extracellular volume fraction for assessing interstitial myocardial fibrosis (Nacif et al., 2012). To acquire contrast-enhanced CT images, iodine-based contrast agent which causes greater absorption

and scattering of x-ray radiation in the target tissue is injected into the blood vessel, and this results in contrast enhancement proportional to the injected iodine concentration (Bae, 2010). The proportionality is nearly constant for a given level of x-ray energy, and the use of a lower level of energy results in stronger contrast enhancement per iodine concentration. As the intracellular uptake of the contrast agent is minimal, contrast enhancement is proportional to the extracellular (vascular and interstitial) concentration of the contrast material (Kormano and Dean, 1976; Miles, 1999). Therefore, hypervascular tumors such as pancreatic neuroendocrine tumors are enhanced by the contrast agent (Miles, 1999; Kazanjian et al., 2006), and the increase in Hounsfield unit indicates the amount of extracellular space. In consequence, the ICVF of the tumor can be computed from the pre- and post-contrast CT images.

To compute the ICVF of the tumor, the pre-contrast CT image is first registered to the post-contrast CT image using deformable image registration based on mutual information (Pluim et al., 2003), and then the difference image is computed to provide the enhancement in Hounsfield unit. As different iodine concentrations and x-ray energy levels provide different contrast enhancements, a known reference of contrast enhancement per iodine concentration, and thus per extracellular space volume, is required. The reference we use is the hematocrit (*Hct*), which is the ratio of the volume of red blood cells to the volume of blood. *Hct* is measurable from patient's blood samples, however, as the records are not always available, the value of 0.45 is used in this paper (Germann and Stanfield, 2005). Using also the contrast enhancement at blood pools such as the aorta, the ICVF ($\theta \in [0, 1]$) of the tumor can be computed as (Liu et al., 2014):

$$\theta = 1 - \frac{HU_{\text{post\_ tumor}} - HU_{\text{pre\_ tumor}}}{\mathrm{E}[HU_{\text{post\_ blood}} - HU_{\text{pre\_ blood}}]}(1 - Het) \quad (8)$$

where $HU_{\text{post\_tumor}}$, $HU_{\text{pre\_tumor}}$, $HU_{\text{post\_blood}}$, and $HU_{\text{pre\_blood}}$ are the Hounsfield units of the post- and pre-contrast CT images at the segmented tumor and blood pool (aorta) (Figure 2). Therefore, the ICVF of the tumor is computed using the ICVF of the blood (*Hct*) as a reference. The computed ICVF can then be used to provide the initial conditions in (2) during simulation, and can be used as the measurements during model personalization.

3.2. Proliferation Rates from FDG-PET Images

Proliferation rates are important factors of tumor growth, and PET images can provide the corresponding functional information. For cells to grow, energy and materials are transported through hierarchical branching networks to the cells and are transformed into metabolic energy for life-sustaining activities. Energy provided to tissues can be divided into two parts, one for maintaining existing cells and another for creating new cells (West et al., 2001). Therefore, the incoming rate of energy flow (B) can be represented as:

$$B = B_c K\theta + E_c K\frac{\partial \theta}{\partial t} \quad (9)$$

where B_c is the metabolic rate of a single cell, E_c is the metabolic energy required to create a cell, and K is the carrying capacity. As $\frac{\partial \theta}{\partial t}$ in (9) only accounts for cell creations, with the assumption of local logistic tumor proliferation, $\frac{\partial \theta}{\partial t} = \rho\theta(1-\theta)$ can be substituted into (9) and the equation becomes:

$$\rho = \frac{B - B_c K\theta}{E_c K\theta(1-\theta)} \quad (10)$$

As B is the overall metabolic rate, its value can be inferred from FDG-PET images. FDG is a biomarker of glucose uptake and metabolism, as it initially follows the same metabolic pathway as glucose (Kelloff et al., 2005). Therefore, FDG-PET images can provide valuable functional information of increased glucose uptake and glycolysis of cancer cells for metabolic abnormalities. To compensate the variation of injected dose and patient weight, the standardized uptake value is usually computed (Thie, 2004) (Figure 2):

$$SUV = \frac{PET}{\text{injected dose/body weight}} \quad (11)$$

with PET the radioactivity concentration provided as the FDG-PET image intensity. As SUV is directly proportional to tissue glucose metabolism (Sadato et al., 1998; Thie, 2004), we can rewrite (10) in the form:

$$\rho = \frac{\alpha SUV - \beta\theta}{\theta(1-\theta)}; \text{with} \alpha SUV = \frac{B}{E_c K} \text{and} \beta = \frac{B_c}{E_c} \quad (12)$$

where $\alpha > 0$ and $\beta > 0$ are unknown scalars to be estimated. $B = \alpha E_c K SUV$ indicates that the overall metabolic rate is proportional to SUV. Therefore, the proliferation rate (ρ) can be approximated from CT and PET images measured at the same time point. With (2), (8), (12), physiologically meaningful quantities can be computed from CT and PET images and combined for better patient-specificity.

4. Model Personalization

Model personalization provides personalized model parameters from image-derived information. For accurate and robust parameter estimation, both the objective function and optimization algorithm should be properly considered.

4.1. Objective Function

To fully utilize the available measurements to improve the subject-specificity of the personalized model, our objective function accounts for both the ICVF and volume differences. The simulation with model parameters×is rasterized into an ICVF image using the CT image at the same time point as a reference, and the following objective function is computed:

$$f(\mathbf{x}) = w_{\mathrm{RMSE}} \sqrt{\mathrm{E}\left[\left(\bar{\theta} - \theta(\mathbf{x})\right)^2\right]} + w_{\mathrm{VD}}(1 - recall + 1 - precision); \quad (13)$$

$$recall = TPV / V_{\mathrm{m}}; precision = TPV / V_{\mathrm{s}}$$

where *TPV* is the true positive volume, the overlapping volume between the simulated tumor volume (V_{s}) and the measured (segmented) tumor volume (V_{m}). In the rasterized ICVF image, we define the tumor voxels as those with ICVF larger than 50%, as almost all image-derived ICVF are larger than this value (Table 3). In consequence, V_{s} is the sum of the volumes of the tumor voxels. $\bar{\theta}$ and $\theta(\mathbf{x})$ are the respective measured and simulated ICVF within *TPV*. Therefore, the objective function accounts for both the ICVF root-mean-squared error (RMSE) and volume difference (VD), and w_{RMSE} and w_{VD} control their respective contributions. In the RMSE term of (13), the square root is necessary to ensure its value is not too small to be useful.

During the personalization process, the model parameters given by the optimization algorithm may not be compatible to each other. For example, the force scaling parameter may be too large and the simulation of the mechanical part may fail. To handle this situation, we can set the objective function to a predefined maximum value. As the maximum value of the RMSE term is one and that of the VD term is two, we can set $f(\mathbf{x}) = w_{\mathrm{RMSE}} + 2w_{\mathrm{VD}}$ if the simulation fails and the objective function cannot be evaluated. The existence of such an upper bound is a merit of the proposed objective function.

Apart from (13) which uses the volume difference explicitly, we also tested another objective function which implicitly accounts for the volume difference:

$$f(\mathbf{x}) = \sqrt{\mathrm{E}\left[\left(g(\bar{\theta}) - g(\theta(\mathbf{x}))\right)^2\right]}, \text{with} g(\theta) = \begin{cases} \theta, & \text{if inside tumor} \\ 0 & \text{if outside tumor} \end{cases} \quad (14)$$

where $\bar{\theta}$ and $\theta(\mathbf{x})$ of the whole image region are considered. This mimics the objective function used in Liu et al. (2014).

4.2. Derivative-Free Global Optimization

The gradient of the objective function (13) is difficult to derive analytically. First of all, although the RMSE term is differentiable with respect to θ, the derivatives of θ with respect to the parameters x are difficult to obtain. Secondly, for the VD term, the analytical derivatives of *recall* and *precision* are nontrivial and may not exist.

To handle this condition, one possible way is to use the finite difference approach (Rao, 2009), which is a popular alternative when analytical gradient is unavailable. Nevertheless, as at least $n + 1$ function evaluations are required, with n the number of parameters, this approach is computationally infeasible. Furthermore, finite difference is sensitive to the step size and may lead to numerical instability. Therefore, it is not the optimal choice to our problem.

Another possible way is to use derivative-free optimization (Conn et al., 2009). There are different algorithms, some with assumptions which can lead to fast convergence if conditions are fulfilled; some with fewer assumptions, which are relatively slow but more precise under most conditions. For example, the BOBYQA (Bound Optimization BY Quadratic Approximation) algorithm solves the local optimization problem by approximating the objective function using a quadratic model through interpolation (Powell, 2009). This algorithm works well with objective functions which are locally quadratic, however, the results of other types of objective functions are less optimal.

Therefore, algorithms that make few assumptions about the objective function should be used. In our early trials, the subplex method (SUBPLEX) was adopted (Rowan, 1990), which is a generalization of the Nelder-Mead simplex method (NMS) (Nelder and Mead, 1965). A simplex in n-dimensional space is a convex hull of $n + 1$ points, for example, a triangle in 2D. In NMS, a simplex moves through the objective function space, changing size and shape, and shrinking near the minimum. SUBPLEX improves NMS by decomposing the searching space into subspaces for better computational efficiency.

Although SUBPLEX is derivative-free with few assumptions of the objective function, we found in the experiments on synthetic data that (see Section 6.2), the model personalization is dependent on the initial parameters (Figure 3). In view of this issue, as our current concentration is on the accuracy and robustness but not speed, the global optimization algorithm DIRECT (DIviding RECTangles) has been adopted (Gablonsky and Kelley, 2001). DIRECT is a sampling algorithm thus does not require the gradient of the objective function. It is a deterministic algorithm which systematically divides the search domain into smaller hyperrectangles, and is designed to completely explore the variable space for the global minimum. With this algorithm, the model personalization can be performed with intact model nonlinearity and increased accuracy, although the computational complexity increases.

5. Sensitivity Analysis

As the tumor growth model comprises various parameters controlling different physiological behaviors, it is advantageous to better understand how the changes of parameters affect the outputs of the model. A useful tool is sensitivity analysis, which assesses how variations in model outputs can be apportioned, qualitatively or quantitatively, to different input sources. It may also reveal the dominant parameters to be varied when generating the synthetic ground truths for the experiments, and the parameters to be optimized in the model personalization.

5.1. Extended Fourier Amplitude Sensitivity Test

The extended Fourier amplitude sensitivity test (eFAST) was used to perform the sensitivity analysis (Marino et al., 2008). eFAST is a variance decomposition method, for which input parameters are varied and causing variation in the model output. The algorithm partitions the output variance to determine the fraction which can be explained by the variation in each input parameter. The partitioning of variance is achieved by varying different parameters at different frequencies, so that the identity of a parameter is encoded in its frequency of

variation. Fourier analysis then measures the strength of each parameter frequency in the model output, and the model sensitivity to a parameter is measured as how strongly the parameter frequency propagates from the input to the output through the model.

eFAST defines a sinusoidal function of a particular frequency for each input parameter with sampling size (N_S). To avoid the inefficiency caused by repeated samples because of the symmetric properties of trigonometric functions, each sinusoidal function is resampled by N_R times with random phase shifts. As such sampling repeats for each parameter analysis, the total number of model simulations is $N_S \times N_R \times n$ for n parameters of interest. At output, eFAST provides two indices to each parameter analyzed. The first-order sensitivity index S indicates the contribution of the parameter of interest to the output variation, which is calculated as its output variance divided by the total variance. The total-order sensitivity index is given as $S_T = 1 - S_C$, with S_C the sum of the output variances of the complement parameters divided by the total variance. Therefore, S_T ($\geq S$) indicates both the contribution of the parameter of interest and its higher-order and nonlinear interactions with the complement parameters.

In our experiments, we used $N_S = 129$ and $N_R = 3$ chosen empirically. Two outputs were studied, which correspond to the average ICVF and the tumor volume:

$$h_{\mathrm{ICVF}} = \mathrm{E}[g(\theta)] - \mathrm{E}[g(\bar{\theta})]; h_{\mathrm{Vol}} = V_s - V_m \quad (15)$$

with θ and V_s the simulated ICVF and tumor volume, and $\bar{\theta}$ and V_m the referencing ICVF and tumor volume before the simulation. The function $g(\bullet)$ is defined in (14). All ten model parameters, D_x, D_y, D_z, α, β, γ, $\lambda_{\mathrm{tissue}}$, μ_{tissue}, λ_{tumor}, μ_{tumor}, were studied. The total computation time was about 24 hours without parallelization.

5.2. Test Results

Table 1 shows that the proliferation parameters α and β were the most dominant parameters to both the ICVF and tumor volume. The next important parameters were the three diffusion coefficients D_x, D_y, D_z, which had larger influence to the ICVF but smaller influence to the tumor volume. The mechanical parameters were the least dominant, while the force scaling parameter γ had higher impact than the passive parameters, especially when the interactions with other parameters were considered.

In consequence, D_x, D_y, D_z, α, and β should be estimated during model personalization. For the mechanical parameters, the force and stiffness are theoretically inseparable for static analysis as any proportional force and stiffness produce the same deformation. As the stiffness properties of pancreatic tissues and tumors are better studied than the growing force, and also because of their relatively low impacts indicated by the sensitivity analysis, we adopted the stiffness parameters from Stylianopoulos et al. (2012), with $\mu_{\mathrm{tissue}} = 1.0$ kPa, $\mu_{\mathrm{tumor}} = 5.0$ kPa, and $\lambda_{\mathrm{tissue}} = \lambda_{\mathrm{tumor}} = 5.0$ kPa. Therefore, the parameters to be estimated were $\mathbf{x} = \{D_x, D_y, D_z, \alpha, \beta, \gamma\}$.

6. Experiments and Results

The proposed framework and other frameworks were tested on synthetic and clinical data to study the differences between using different biomechanical models and between using different objective functions. The tested frameworks were:

- **Nonlinear root-mean-squared error (RMSE) and volume difference (VD) (N-RMSEVD)**: the proposed framework with nonlinear biomechanics (3) and with $w_{\text{RMSE}} = w_{\text{VD}} = 1$ in (13).
- **Nonlinear VD (N-VD)**: same as N-RMSEVD but only the volume difference was considered in the objective function, i.e. $w_{\text{RMSE}} = 0$ and $w_{\text{VD}} = 1$ in (13).
- **Nonlinear RMSE (N-RMSE)**: same as N-RMSEVD but using the objective function in (14), which accounts for the volume difference implicitly through the ICVF RMSE.
- **Linear RMSE and VD (L-RMSEVD):** same as N-RMSEVD but using the Hooke's law in (6). The Young's moduli (E) of the tissue and tumor were 1.0 and 5.0 kPa, respectively. Poisson's ratios $\nu = 0.45$ for linear model incompressibility.

Measurements at three time points were required in each experiment. Simulation was initiated on the model at the first time point, with the ICVF and SUV images providing the initial conditions and proliferation rates in (2). The simulated model was rasterized and compared with the measured ICVF and tumor volume at the second time point to evaluate the objective function for parameter estimation. Prediction was performed by simulating the tumor growth using the personalized model, with the FEM mesh, ICVF, and SUV at the second time point as the inputs. The prediction performance was evaluated using the measurements at the third time point, and it was represented as recall, precision, Dice coefficient, relative volume difference (RVD), average surface distance (ASD), and ICVF root-mean-squared error (RMSE). Recall, precision, and RMSE are defined in (13). To compute ASD, for each node on the simulated tumor surface, its absolute distance to the nearest node on the measured tumor surface is computed. ASD is the average of all these distances of all nodes. Dice coefficient and RVD are defined as:

$$\text{Dice}=\frac{2\times TPV}{V_s+V_m};\text{RVD}=\frac{|V_s-V_m|}{V_m} \quad (16)$$

with TPV, V_s, and V_m defined in (13).

Please note that as the models and implementations between this work and Liu et al. (2014) are very different, and as the data sets are only partially overlapped because of the addition and removal of data based on the availability and framework requirements, their results cannot be fairly compared.

6.1. Tumor Segmentation, Registration, and Meshing

The tumor volumes at all time points were segmented from the post-contrast CT images by a level set algorithm with region competition in ITK-SNAP (Yushkevich et al., 2006). For each data set, using the segmented tumor at the first time point as a reference, PET images

and segmented tumors at other time points were center-aligned through rigid registration to preserve the sizes of the tumors, and the corresponding SUV and ICVF were computed (Figure 2). Center-alignment was used as the pancreas is highly deformable, and thus it is difficult to accurately align the tumors using the surrounding features. Linear tetrahedral FEM meshes (3.2 to 4.5 × 10^4 elements) were built from the segmented tumors and their surrounding tissues using iso2mesh (Fang and Boas, 2009) (Figure 2).

6.2. Synthetic Data

6.2.1. Experimental Setups—We studied the parameter estimation capability using synthetic data. Using the FEM mesh, SUV, and ICVF images of a patient at the first time point (Day 0, Figure 4(a)), the tumor at the second time point (Day 300) was simulated with the ground-truth model parameters using the proposed model (Table 2). This FEM simulation was rasterized into an ICVF image which was used as the input to the experiments (Figure 4). The estimated parameters were then used to predict the tumor at the third time point (Day 600), which was compared with the simulated ground truth for the prediction performance. As the rasterized image lost all deformation information and some ICVF information of the FEM simulation, the parameter estimation is nontrivial.

To study the performances at different growth rates, simulated ground truths with different model parameters were produced. The baseline parameters were $\{D_x, D_y, D_z\}$ = {2.0, 1.0, 0.0} × 10^{-3} mm^2/day, α = 3.5 mm^3/g/day, β = 2.0 × 10^{-2} day^{-1}, and γ = 2.0 kPa. As the sensitivity analysis in Section 5 shows that the SUV scaling parameter α is the most dominant parameter for tumor growth, we simulated ground truths with α = 2.5, 3.0, 3.5, and 4.0 mm3/g/day. We also simulated ground truths with γ = 1.0, 2.0, 3.0, and 4.0 kPa to study the performances under different magnitudes of mass effect (Figure 4). Consistent with the sensitivity analysis, Figure 5 shows that the tumor growth was more sensitive to α, though γ should also be considered for more accurate results.

For the model personalization, DIRECT does not require the initial values of the parameters but their lower and upper bounds. In our experiments on synthetic data, $\{D_x, D_y, D_z\} \in$ [0.0, 5.0] × 10^{-3} mm^2/day, $\alpha \in$ [0.0, 5.0] mm^3/g/day, $\beta \in$ [0.0, 5.0] × 10^{-2} day^{-1}, and $\gamma \in$ [0.0, 5.0] kPa. The maximum number of function evaluations was 2,000. As accuracy is more important than computational time in these experiments, a conservative convergence criterion was used, with the objective function value less than 10−3 to stop the optimization.

6.2.2. Results—Table 2 shows the estimated parameters and the prediction performances for synthetic data, and Figure 6 shows the differences between the estimated and ground-truth parameters. For parameters α and β, the estimated values of all frameworks were similar in general. The estimated values of β were mostly around 2.5 ×10^{-2} day^{-1} to compensate for the estimated values of α that were mostly around 0.6 mm3/g/day larger than the ground-truth values (Table 2(a) and (b)). When the ground-truth α = 4.0 mm^3/g/day, the estimated values of β were close to 0.8 × 10^{-2} day^{-1} to compensate for the underestimated α with values around 2.5 mm^3/g/day (Table 2(a)). Despite these differences from the ground truths, the prediction performances, especially those of the N-RMSEVD and L-RMSEVD frameworks, were nearly perfect. This means that different combinations

of α and β can lead to similar proliferation rates, and thus they are not totally separable. In fact, this property can be inferred from (12). With known *SUV* and θ from the measurements, (12) is a plane in 3D space, and any α and β on the same contour contribute to the same proliferation rate. Nevertheless, as both α and β are dominant parameters to the tumor growth model, we prefer to estimate them together until a formal solution is found.

For the other parameters, the N-RMSEVD framework had the best estimation by using the ground-truth model and the complementary measurements from the ICVF images and tumor volumes. In consequence, it had the best prediction performance among the tested frameworks. For the N-VD and N-RMSE frameworks, their estimated diffusion coefficients had the largest differences from the ground truths. The N-RMSE framework had the worst prediction performance, with the minimum Dice coefficient as 79.6% and the maximum RVD as 33.8%. This shows that the implicit use of tumor volumes through ICVF (i.e. N-RMSE) is worse than explicitly comparing both the ICVF and tumor volumes (i.e. N-RMSEVD). For the L-RMSEVD framework, it had similar capability as the N-RMSEVD framework on estimating the diffusion parameters, but it had the largest difference for the force scaling parameter (γ) to compensate for the mechanical model mismatch. Despite this large force scaling difference, its prediction performance was better than those of the N-VD and N-RMSE frameworks. This shows that complementary measurements are more important than the biomechanical model. In fact, the small performance difference between the N-RMSEVD and L-RMSEVD frameworks is consistent with the results of the sensitivity analysis that, the force scaling parameter is not a dominant factor in our model.

Although the N-RMSEVD framework had the best results, other frameworks also had good performances. This is reasonable as the frameworks were only incrementally different from each other. As all frameworks used the same optimization algorithm, this shows that the DIRECT optimization is appropriate for our chosen objective function, and can provide accurate results when the models can properly account for the underlying physiological status. Nevertheless, as model uncertainties exist in reality, the performances on the clinical data were less optimal.

6.3. Clinical Data

6.3.1. Experimental Setups—Images from eight patients (five males and three females) with eight diagnosed pancreatic neuroendocrine tumors were used. In this IRB-approved protocol for investigation of disease nature, there were no treatments to the tumors until they reached 3 cm in diameter. The average age and weight of the patients at the first time point were 49.6±13.2 years and 84.9±17.8 kg, respectively. Each set of data had three time points of contrast-enhanced CT and FDG-PET images spanning three to four years, and the pixel sizes were less than $0.94 \times 0.94 \times 1.00$ mm^3 and $4.25 \times 4.25 \times 3.27$ mm^3, respectively. Table 3 shows the tumor information of all patients at different time points. Some patients had similar time spans between the measurements, while some were very different. There were also different tumor sizes and maximum SUV values, and the ICVF values were mostly between 50% and 90%.

For the model personalization, the ranges of the model parameters were double of those of the synthetic data, as larger variations were expected. Therefore, $\{D_x, D_y, D_z\} \in [0.0, 10.0]$

$\times 10^{-3}$ mm^2/day, $\alpha \in [0.0, 10.0]$ mm^3/g/day, $\beta \in [0.0, 10.0] \times 10^{-2}$ day^{-1}, and $\gamma \in [0.0, 10.0]$ kPa. The maximum number of function evaluations was 2,000, and the objective function value had to be smaller than 10^{-3} for convergence.

6.3.2. Results—Table 4 shows the estimated parameters and the prediction performances of different frame-works. As the actual parameter values were unavailable, numerical evaluation of the estimated parameters was impossible, though the prediction performances could still be verified. Table 4(a) shows that, similar to the synthetic data, the N-RMSEVD framework had the best prediction performance. Nevertheless, different from the synthetic data, the prediction performance of the L-RMSEVD framework was poor as there was an outlier to the results. The outlier was Patient 7, whose RVD was 474.6%. The actual reason of this outlier is unclear, though Table 3 shows that Patient 7 had the largest time difference ratio between the measurement time points (552 to 168 days) while the percentage growths were similar. Figure 7 shows the predicted tumor volumes and ICVF of Patient 7, whose data set also contributed to the worst case of the N-VD framework.

Figure 8 shows the results of Patient 4, an example of good prediction. Figure 8(a) and Table 3 show that the tumor size and ICVF increased consistently from the first to the third time point. Therefore, the model personalized using the measurements at the first and second time points could properly predict the tumor growth at the third time point. On the other hand, Figure 9 shows the results of Patient 6, the worst case apart from the outlier. Figure 9(a) and Table 3 show that the tumor size and ICVF increased from the first to the second time point, but decreased at the third time point. Therefore, the personalized models overestimated the tumor size and ICVF.

To better compare the frameworks, Patient 7 was removed from the data sets, and the updated prediction performances are show in Table 4(b). After removing the outlier, the differences among the frameworks were more similar to those of the synthetic data. The prediction performances of the N-VD and N-RMSE frameworks were similar, and they were worse than those of the N-RMSEVD and L-RMSEVD frameworks which had similarly good performances. Except the recall and RMSE which were similar in all frameworks, other scores of the N-VD and N-RMSE frameworks were worse than those of the N-RMSEVD and L-RMSEVD frameworks. Especially for the RVD, the maximum values of the N-VD and N-RMSE frameworks were up to 60%. These again show the importance of the complementary ICVF and tumor volume information for accurate tumor growth personalization. Comparing between the N-RMSEVD and L-RMSEVD frameworks, similar to the synthetic data, the force scaling parameters γ estimated by the L-RMSEVD framework were larger than those of the N-RMSEVD framework to compensate for the model difference. Regardless of such a difference, both the N-RMSEVD and L-RMSEVD frameworks had promising performances, with the average Dice coefficients around 85% and the average RVD less than 15%. This implies that for the predictions of slow growing tumors, the use of a linear mechanical model with lower computational complexity can be appropriate, though the outliers (e.g. Figure 7) can have larger effect on the linear model.

7. Discussion

Comparing with other works, this paper presents a relatively complete evaluation of the parameter estimation capability and prediction performance of the proposed framework. For example, the works of Chen et al. (2013) and Liu et al. (2014) did not have experiments on synthetic data, and thus the accuracy and robustness of the parameter estimations were unknown, and the potential pitfalls such as the uniqueness of the estimated parameters were not studied. On the other hand, while the works of Hogea et al. (2008) and Konukoglu et al. (2010) had relatively detailed evaluations of the parameter estimations through synthetic data, the evaluations of the prediction capability on clinical data were limited. In contrast, we provide detailed evaluation of the parameter estimation capability on synthetic data, highlight the potential pitfalls, and compare among different mechanical models and objective functions. We also provide detailed prediction performance evaluation on clinical data through different metrics such as the Dice coefficient and relative volume difference, and analyze the possible causes of the good and bad results. Therefore, our framework is properly evaluated through both synthetic and clinical data.

The prediction performance of our framework is promising, with the average Dice coefficient as 84.6±1.7% on the clinical data. This performance is comparable to those of the state-of-the-art automatic tumor segmentation algorithms (Massoptier and Casciaro, 2008; Han et al., 2011; Hamamci et al., 2012) even though we did not use any image information of the target tumors during prediction. Although the nature of our work is different from that of the automatic tumor segmentation, this gives an idea of the promising prediction capability of our framework.

To visualize cellular proliferation, [^{18}F]-fluoro-3′-deoxy-3′-L-fluorothymidine (FLT) PET tracer is available for noninvasive imaging of tumor cell proliferation (Been et al., 2004). Nevertheless, comparing with FDG, FLT uptake is lower in most cases and does not always reflect the tumor cell proliferation rates. Furthermore, FLT-PET is not a common clinical practice. Therefore, we utilize the widely-used FDG-PET images to compute the proliferation rates instead.

A limitation of this paper is the availability of the measurements. Although using more time points can improve the prediction accuracy, as the FDG-PET images are not always available, only two time points are used for the model personalization. In consequence, when the growth from the first to the third time point is inconsistent, such as the case of Patient 6, large prediction errors may occur. Furthermore, as pancreatic neuroendocrine tumors are slow growing, the prediction performance of our framework on fast growing tumors cannot be validated using the clinical data.

In the future, we will improve both the reaction-diffusion equation and the mechanical model. In our current reaction-diffusion equation, we only consider cell proliferation but not reduction in the reaction term. As our data are from patients without treatments, this model is still appropriate. Nevertheless, if treatment efficacy or tumor necrosis need to be considered, extra terms accounting for these conditions need to be included. This can further

improve the clinical applicability of the framework and can lead to valuable applications such as cancer drug study.

For the mechanical model, although the hyperelastic constitutive law is used for more realistic passive mechanical behavior, the use of the ICVF gradient for the outward pushing force of the tumor may be less optimal. First of all, the rate of the tumor size change caused by mass effect cannot be explicitly included. Furthermore, modeling the tumor size change as elastic response contradicts the nearly incompressible nature of most solid tumors, and thus the incompressibility of the mechanical model needs to be compromised. To improve the realism of the mass effect modeling, approaches of multiplicative growth decomposition such as those discussed in Menzel and Kuhl (2012) will be considered.

8. Conclusion

In this paper, we have proposed a pancreatic neuroendocrine tumor growth prediction framework which comprises a FEM-based growth model with coupled reaction-diffusion equation and nonlinear biomechanics. With the derivative-free global optimization algorithm DIRECT, the complementary information from contrast-enhanced CT and FDG-PET images are physiologically fused together to personalize the model with improved patient-specificity. The sensitivity analysis of the model shows that the parameters of the reaction-diffusion equation are more dominant than those of the biomechanical model. The results of the synthetic data demonstrate the parameter estimation capability of our framework, and the results of the clinical data show its promising prediction performance.

Acknowledgements

This work was funded by the Intramural Research Program of the National Institutes of Health Clinical Center.

References

Alarcón T, Byrne HM, Maini PK. A cellular automaton model for tumour growth in inhomogeneous environment. Journal of Theoretical Biology. 2003; 225:257–274. [PubMed: 14575659]

Ambrosi D, Mollica F. On the mechanics of a growing tumor. International Journal of Engineering Science. 2002; 40:1297–1316.

Bae KT. Intravenous contrast medium administration and scan timing at CT: considerations and approaches. Radiology. 2010; 256:32–61. [PubMed: 20574084]

Bathe, KJ. Finite Element Procedures. Prentice Hall; 1996.

Been LB, Suurmeijer AJH, Cobben DCP, Jager PL, Hoekstra HJ, Elsinga PH. [18F] FLT-PET in oncology: current status and opportunities. European Journal of Nuclear Medicine and Molecular Imaging. 2004; 31:1659–1672. [PubMed: 15565331]

Blansfield JA, Choyke L, Morita SY, Choyke PL, Pingpank JF, Alexander HR, Seidel G, Shutack Y, Yuldasheva N, Eugeni M, Bartlett DL, Glenn GM, Middelton L, Linehan WM, Libutti SK. Clinical, genetic and radiographic analysis of 108 patients with von Hippel-Lindau disease (VHL) manifested by pancreatic neuroendocrine tumors (PNETs). Surgery. 2007; 142:814–818. e2. [PubMed: 18063061]

Byrne HM. Dissecting cancer through mathematics: from the cell to the animal model. Nature Reviews Cancer. 2010; 10:221–230. [PubMed: 20179714]

Chen X, Summers RM, Yao J. Kidney tumor growth prediction by coupling reaction-diffusion and biomechanical model. IEEE Transactions on Biomedical Engineering. 2013; 60:169–173. [PubMed: 23047857]

Clatz O, Sermesant M, Bondiau PY, Delingette H, Warfield SK, Malandain G, Ayache N. Realistic simulation of the 3D growth of brain tumors in MR images coupling diffusion with biomechanical deformation. IEEE Transactions on Medical Imaging. 2005; 24:1334–1346. [PubMed: 16229419]

Clayton TA, Lindon JC, Cloarec O, Antti H, Charuel C, Hanton G, Provost JP, Le Net JL, Baker D, Walley RJ, Everett JR, Nicholson JK. Pharmaco-metabonomic phenotyping and personalized drug treatment. Nature. 2006; 440:1073–1077. [PubMed: 16625200]

Conn, AR.; Scheinberg, K.; Vicente, LN. Introduction to Derivative-Free Optimization. Vol. 8. Siam; 2009.

Ehehalt F, Saeger HD, Schmidt CM, Grützmann R. Neuroendocrine tumors of the pancreas. The Oncologist. 2009; 14:456–467. [PubMed: 19411317]

Fang, Q.; Boas, DA. Tetrahedral mesh generation from volumetric binary and grayscale images; IEEE International Symposium on Biomedical Imaging 2009; 2009. p. 1142-1145.

Friedl P, Locker J, Sahai E, Segall JE. Classifying collective cancer cell invasion. Nature Cell Biology. 2012; 14:777–783. [PubMed: 22854810]

Fung, YC. Biomechanics: Mechanical Properties of Living Tissues. 2nd ed.. Springer-Verlag; 1993.

Gablonsky JM, Kelley CT. A locally-biased form of the DIRECT algorithm. Journal of Global Optimization. 2001; 21:27–37.

Gatenby RA, Gawlinski ET. A reaction-diffusion model of cancer invasion. Cancer Research. 1996; 56:5745–5753. [PubMed: 8971186]

Germann WJ, Stanfield CL. Principles of Human Physiology. Pearson Benjamin Cummings. 2005

Graziano L, Preziosi L. Mechanics in tumor growth, in: Modeling of Biological Materials. Birkhäuser Boston. 2007:263–321.

Hamamci A, Kucuk N, Karaman K, Engin K, Unal G. Tumor-cut: segmentation of brain tumors on contrast enhanced MR images for radiosurgery applications. IEEE Transactions on Medical Imaging. 2012; 31:790–804. [PubMed: 22207638]

Han, D.; Bayouth, J.; Song, Q.; Taurani, A.; Sonka, M.; Buatti, J.; Wu, X. Globally optimal tumor segmentation in PET-CT images: a graph-based co-segmentation method. Springer: Information Processing in Medical Imaging; 2011. p. 245-256.

Hogea C, Davatzikos C, Biros G. An image-driven parameter estimation problem for a reaction-diffusion glioma growth model with mass effects. Journal of Mathematical Biology. 2008; 56:793–825. [PubMed: 18026731]

Holzapfel, GA. Nonlinear Solid Mechanics: A Continuum Approach for Engineering. John Wiley & Sons, Inc.; 2000.

Jiang Y, Pjesivac-Grbovic J, Cantrell C, Freyer JP. A multiscale model for avascular tumor growth. Biophysical Journal. 2005; 89:3884–3894. [PubMed: 16199495]

Kam Y, Rejniak KA, Anderson AR. Cellular modeling of cancer invasion: integration of in silico and in vitro approaches. J Cell Physiol. 2012; 227:431–438. [PubMed: 21465465]

Kazanjian KK, Reber HA, Hines OJ. Resection of pancreatic neuroendocrine tumors: results of 70 cases. Archives of Surgery. 2006; 141:765–770. [PubMed: 16924083]

Kelloff G, Hoffman JM, Johnson B, Scher HI, Siegel BA, Cheng EY, Cheson BD, O'Shaughnessy J, Guyton KZ, Mankoff DA, Shankar L, Larson SM, Sigman CC, Schilsky RL, Sullivan DC. Progress and promise of FDG-PET imaging for cancer patient management and oncologic drug development. Clinical Cancer Research. 2005; 11:2785–2808. [PubMed: 15837727]

Konukoglu E, Clatz O, Menze BH, Stieltjes B, Weber MA, Mandonnet E, Delingette H, Ayache N. Image guided personalization of reaction-diffusion type tumor growth models using modified anisotropic eikonal equations. IEEE Transactions on Medical Imaging. 2010; 29:77–95. [PubMed: 19605320]

Kormano M, Dean PB. Extravascular contrast material: the major component of contrast enhancement. Radiology. 1976; 121:379–382. [PubMed: 981616]

Kyriacou SK, Davatzikos C, Zinreich SJ, Bryan RN. Nonlinear elastic registration of brain images with tumor pathology using a biomechanical model. IEEE Transactions on Medical Imaging. 1999; 18:580–592. [PubMed: 10504092]

Liu Y, Sadowski S, Weisbrod A, Kebebew E, Summers R, Yao J. Patient specific tumor growth prediction using multimodal images. Medical Image Analysis. 2014; 18:555–566. [PubMed: 24607911]

Marino S, Hogue IB, Ray CJ, Kirschner DE. A methodology for performing global uncertainty and sensitivity analysis in systems biology. Journal of Theoretical Biology. 2008; 254:178–196. [PubMed: 18572196]

Massoptier L, Casciaro S. A new fully automatic and robust algorithm for fast segmentation of liver tissue and tumors from CT scans. European Radiology. 2008; 18:1658–1665. [PubMed: 18369633]

Menze, BH.; Van Leemput, K.; Honkela, A.; Konukoglu, E.; Weber, MA.; Ayache, N.; Golland, P. A generative approach for image-based modeling of tumor growth. Springer: Information Processing in Medical Imaging; 2011. p. 735-747.

Menzel A, Kuhl E. Frontiers in growth and remodeling. Mechanics Research Communications. 2012; 42:1–14. [PubMed: 22919118]

Miles KA. Tumour angiogenesis and its relation to contrast enhancement on computed tomography: a review. European Journal of Radiology. 1999; 30:198–205. [PubMed: 10452718]

Nacif MS, Kawel N, Lee JJ, Chen X, Yao J, Zavodni A, Sibley CT, Lima JAC, Liu S, Bluemke DA. Interstitial myocardial fibrosis assessed as extracellular volume fraction with low-radiation-dose cardiac CT. Radiology. 2012; 264:876–883. [PubMed: 22771879]

Nelder JA, Mead R. A simplex method for function minimization. Computer Journal. 1965; 7:308–313.

Pluim JPW, Maintz JBA, Viergever MA. Mutual-information-based registration of medical images: a survey. IEEE Transactions on Medical Imaging. 2003; 22:986–1004. [PubMed: 12906253]

Powell, MJD. Cambridge NA Report NA2009/06. Cambridge: University of Cambridge; 2009. The BOBYQA algorithm for bound constrained optimization without derivatives.

Rao, SS. Engineering Optimization: Theory and Practice. John Wiley & Sons, Inc.; 2009.

Ries, LAG.; Young, JL.; Keel, GE.; Eisner, MP.; Lin, YD.; Horner, MJ., editors. SEER Survival Monograph: Cancer Survival Among Adults: U.S. SEER Program, 1988–2001, Patient and Tumor Characteristics. National Cancer Institute, SEER Program, NIH; 2007.

Rogers JM, McCulloch AD. A collocation-Galerkin finite element model of cardiac action potential propagation. IEEE Transactions on Biomedical Engineering. 1994; 41:743–757. [PubMed: 7927397]

Rowan, T. Ph.D. thesis. University of Texas at Austin; 1990. Functional Stability Analysis of Numerical Algorithms.

Sadato N, Tsuchida T, Nakaumra S, Waki A, Uematsu H, Takahashi N, Hayashi N, Yonekura Y, Ishii Y. Non-invasive estimation of the net influx constant using the standardized uptake value for quantification of FDG uptake of tumours. European Journal of Nuclear Medicine. 1998; 25:559–564. [PubMed: 9618569]

Schilsky RL. Personalized medicine in oncology: the future is now. Nature Reviews Drug Discovery. 2010; 9:363–366.

Stylianopoulos T, Martin JD, Chauhan VP, Jain SR, Diop-Frimpong B, Bardeesy N, Smith BL, Ferrone CR, Hornicek FJ, Boucher Y, Munn LL, Jain RK. Causes, consequences, and remedies for growth-induced solid stress in murine and human tumors. Proc. Natl. Acad. Sci. USA. 2012; 109:15101–15108. [PubMed: 22932871]

Thie JA. Understanding the standardized uptake value, its methods, and implications for usage. Journal of Nuclear Medicine. 2004; 45:1431–1434. [PubMed: 15347707]

West GB, Brown JH, Enquist BJ. A general model for ontogenetic growth. Nature. 2001; 413:628–631. [PubMed: 11675785]

Yushkevich PA, Piven J, Hazlett HC, Smith RG, Ho S, Gee JC, Gerig G. User-guided 3D active contour segmentation of anatomical structures: significantly improved efficiency and reliability. NeuroImage. 2006; 31:1116–1128. [PubMed: 16545965]

Highlights

- Tumor growth prediction with physiological data fusion.
- A tumor growth model with reaction-diffusion and hyperelastic biomechanical model.
- A derivative-free global optimization algorithm for model parameter estimation.
- Physiological data fusion of contrast-enhanced CT and FDG-PET images.
- Average prediction performance: Dice = 84.6

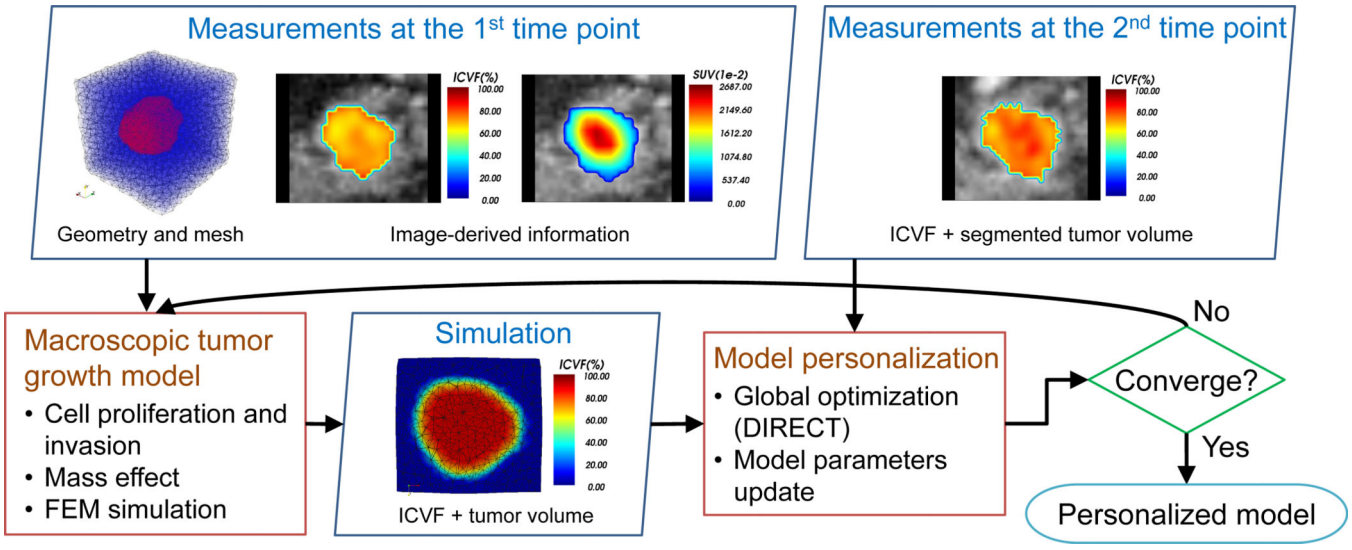

Figure 1.
Model personalization framework.

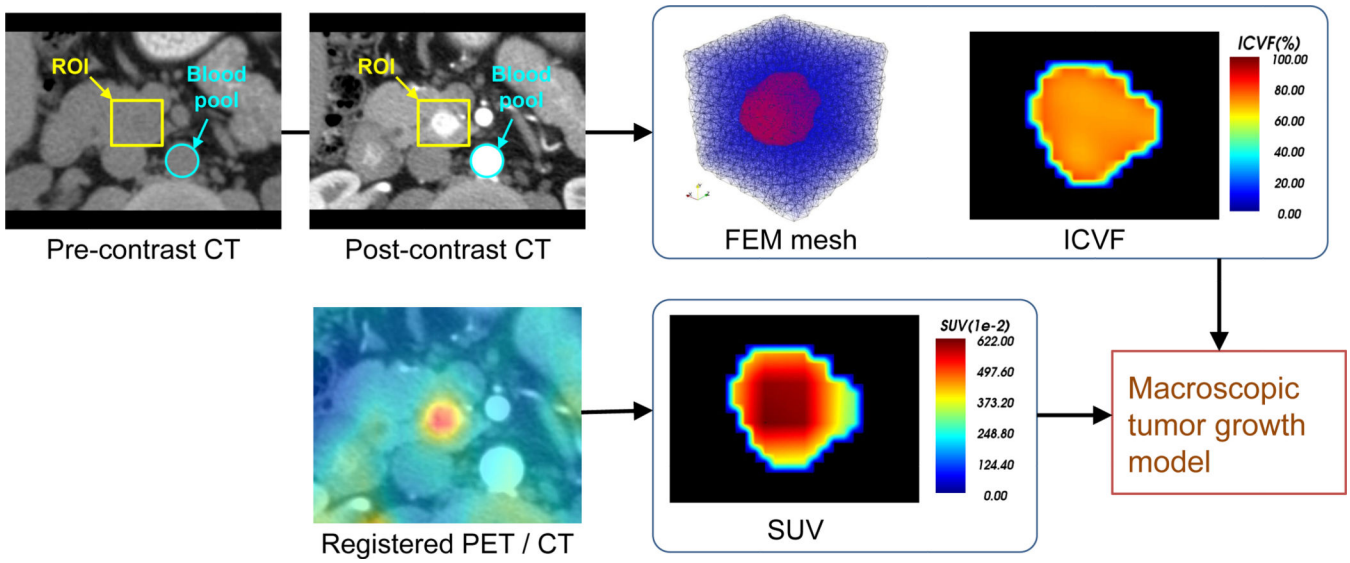

Figure 2.

Image-derived information. The SUV image combines with the ICVF image to provide the proliferation rates through (12). The ICVF image provides the initial conditions of the reaction-diffusion equation (2) and the measurements for model personalization. In the FEM mesh, the tumor is red and the surrounding tissues are blue.

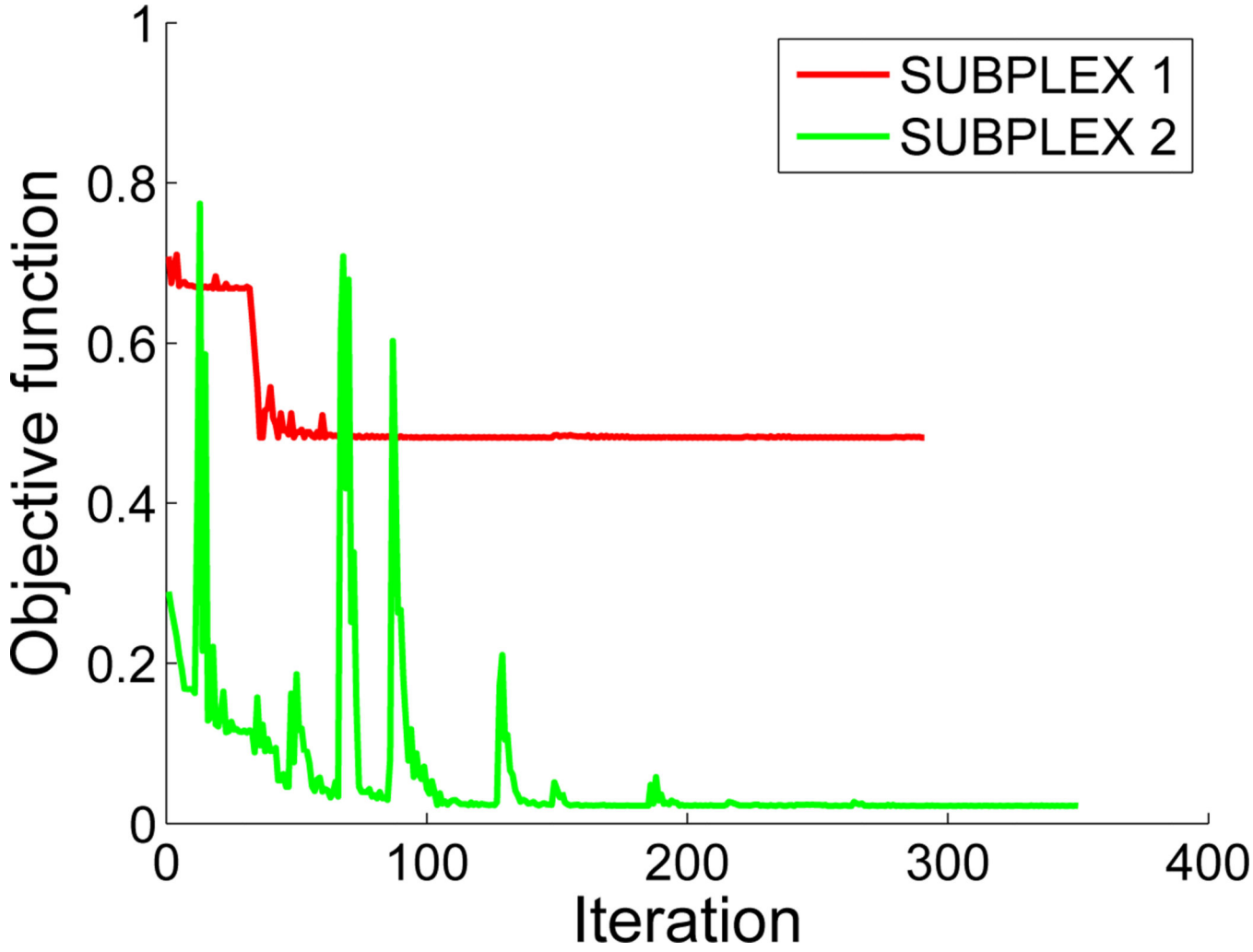

Figure 3.
Objective function evolutions with SUBPLEX. Different initial parameters lead to different results.

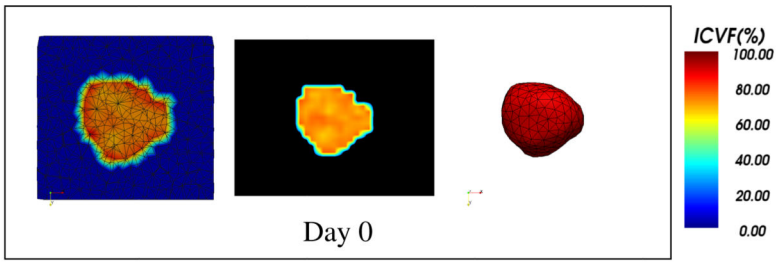

(a) ICVF and tumor volume before simulation.

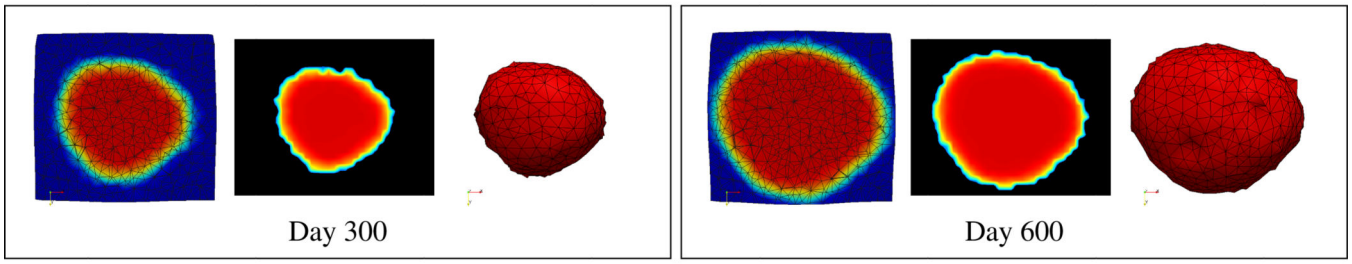

(b) $\alpha = 3.5$ mm^3/g/day, $\gamma = 2.0$ kPa.

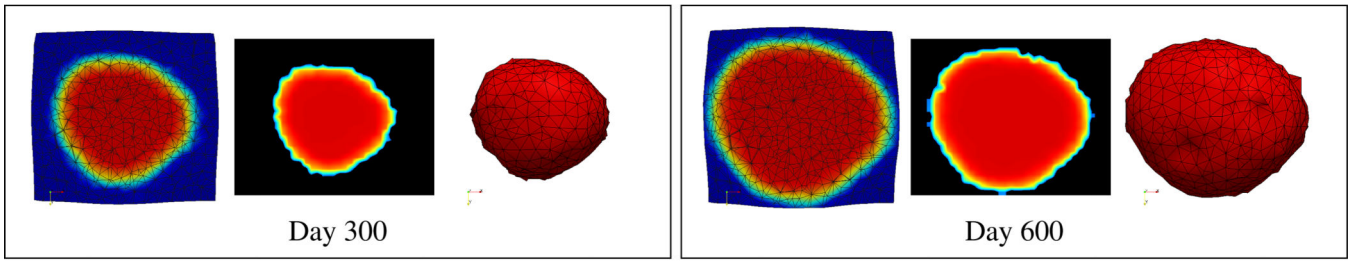

(c) $\alpha = 3.5$ mm^3/g/day, $\gamma = 4.0$ kPa.

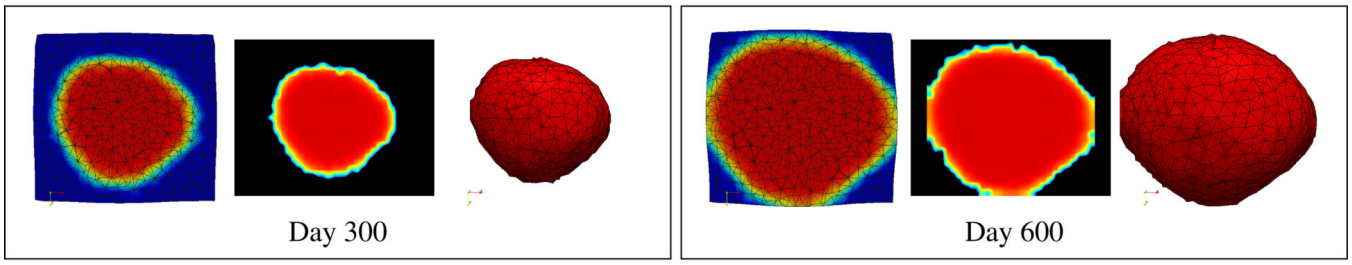

(d) $\alpha = 4.0$ mm^3/g/day, $\gamma = 2.0$ kPa.

Figure 4.

Synthetic data. Tumor growth simulations with different model parameters. Left to right in each box: the FEM representation of ICVF, the rasterized ICVF image, and the tumor volume. (a) Before simulation. (b)–(d) Simulations with different values of SUV scaling parameter (α) and force scaling parameter (γ).

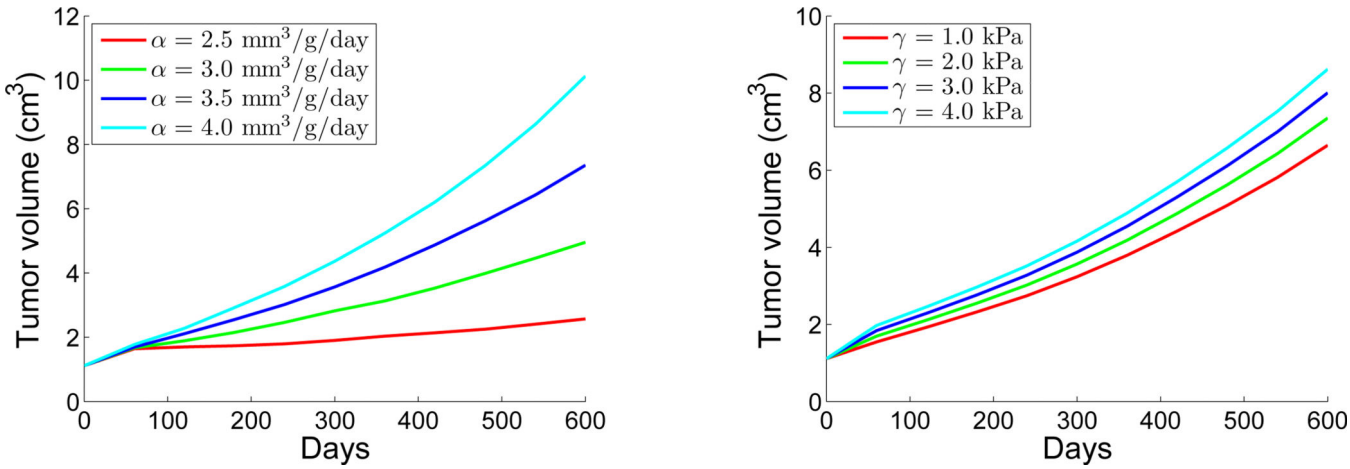

Figure 5.

Synthetic data. Tumor growth curves with different values of SUV scaling parameter (α) and force scaling parameter (γ).

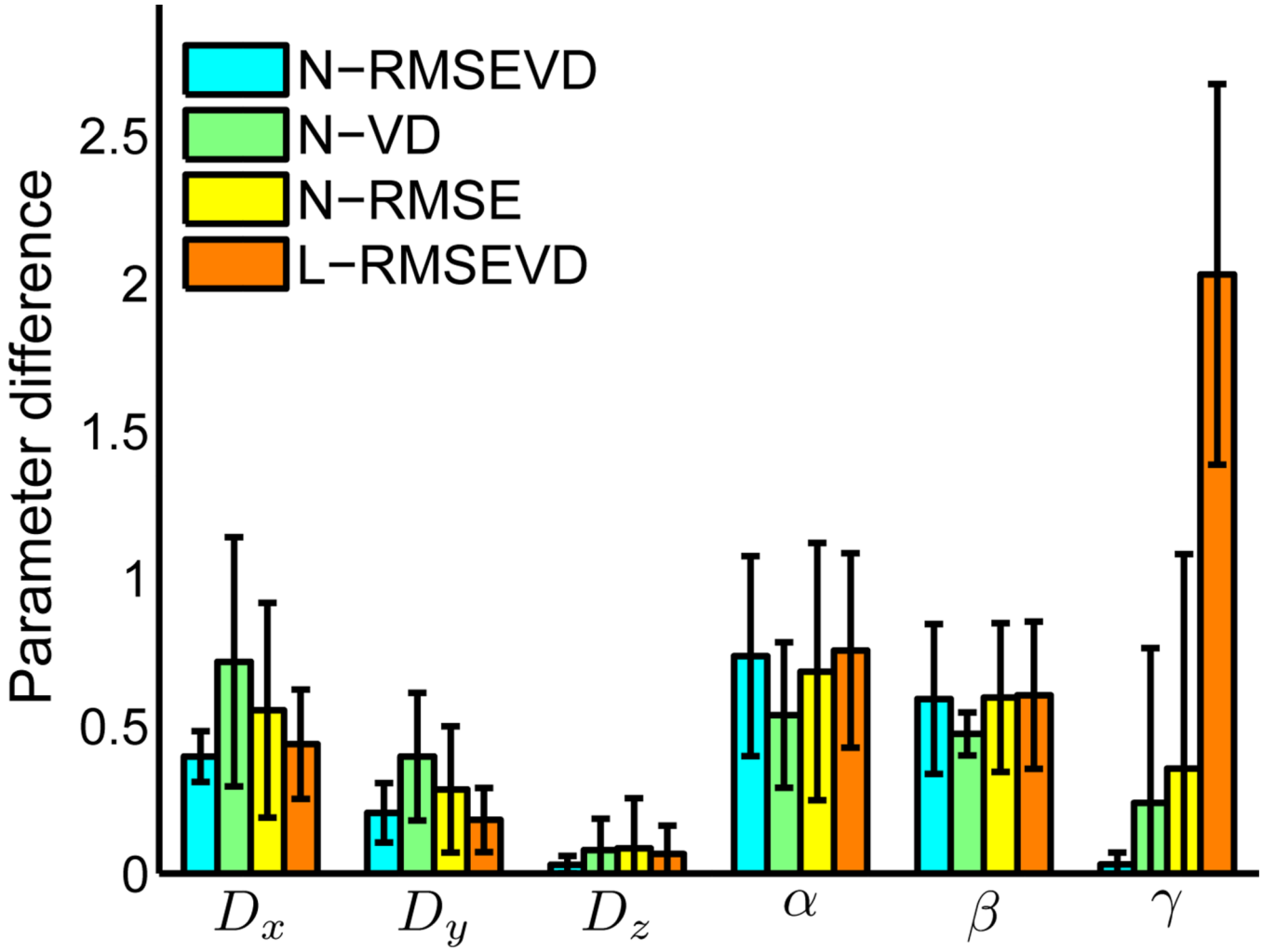

Figure 6.

Synthetic data. Parameter differences between the estimated and ground-truth values. As the ground-truth value of D_z is zero, relative differences cannot be used. The unit of the *y*-axis corresponds to the different units of the model parameters.

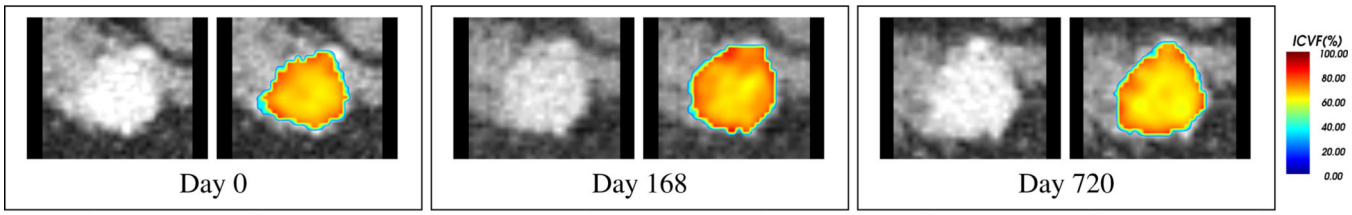

(a) CT and ICVF images at the three measurement time points.

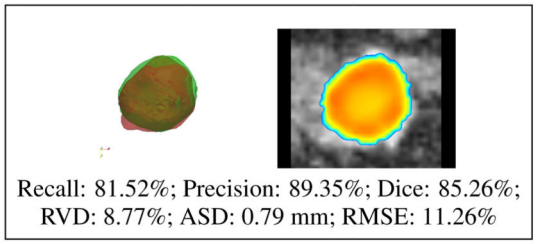

Recall: 81.52%; Precision: 89.35%; Dice: 85.26%; RVD: 8.77%; ASD: 0.79 mm; RMSE: 11.26%

(b) N-RMSEVD.

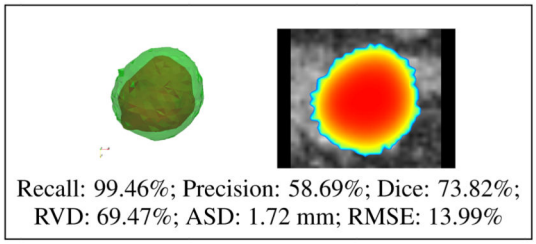

Recall: 99.46%; Precision: 58.69%; Dice: 73.82%; RVD: 69.47%; ASD: 1.72 mm; RMSE: 13.99%

(c) N-VD.

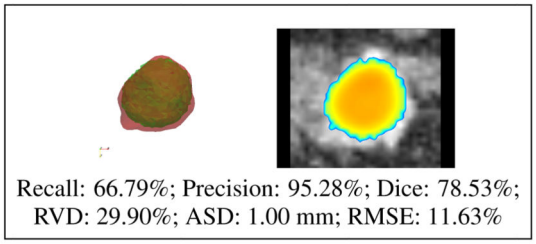

Recall: 66.79%; Precision: 95.28%; Dice: 78.53%; RVD: 29.90%; ASD: 1.00 mm; RMSE: 11.63%

(d) N-RMSE.

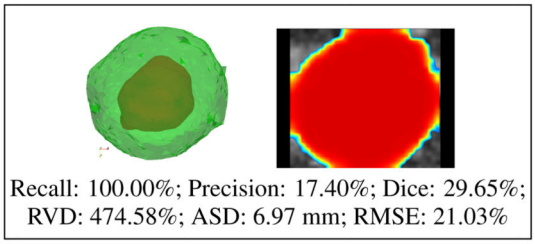

Recall: 100.00%; Precision: 17.40%; Dice: 29.65%; RVD: 474.58%; ASD: 6.97 mm; RMSE: 21.03%

(e) L-RMSEVD.

Figure 7.

Clinical data. Patient 7. (a) CT and ICVF images at the three measurement time points. (b)–(e): prediction at the third time point, with the measured (red) and predicted (green) tumors superimposed.

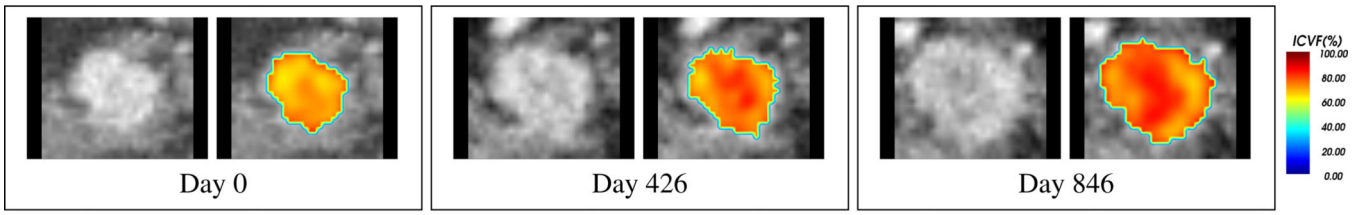

(a) CT and ICVF images at the three measurement time points.

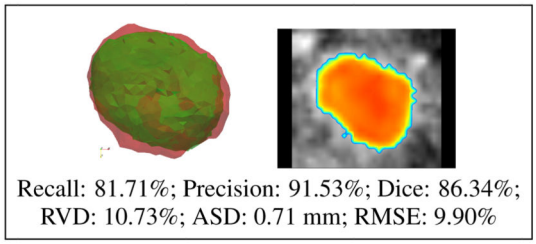

Recall: 81.71%; Precision: 91.53%; Dice: 86.34%; RVD: 10.73%; ASD: 0.71 mm; RMSE: 9.90%

(b) N-RMSEVD.

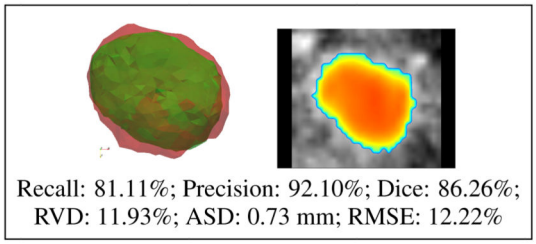

Recall: 81.11%; Precision: 92.10%; Dice: 86.26%; RVD: 11.93%; ASD: 0.73 mm; RMSE: 12.22%

(c) N-VD.

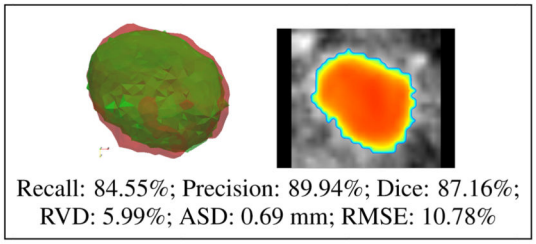

Recall: 84.55%; Precision: 89.94%; Dice: 87.16%; RVD: 5.99%; ASD: 0.69 mm; RMSE: 10.78%

(d) N-RMSE.

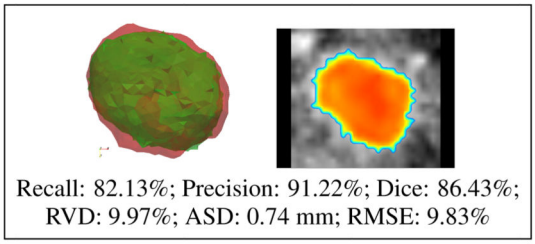

Recall: 82.13%; Precision: 91.22%; Dice: 86.43%; RVD: 9.97%; ASD: 0.74 mm; RMSE: 9.83%

(e) L-RMSEVD.

Figure 8.

Clinical data. Patient 4. (a) CT and ICVF images at the three measurement time points. (b)–(e): prediction at the third time point, with the measured (red) and predicted (green) tumors superimposed.

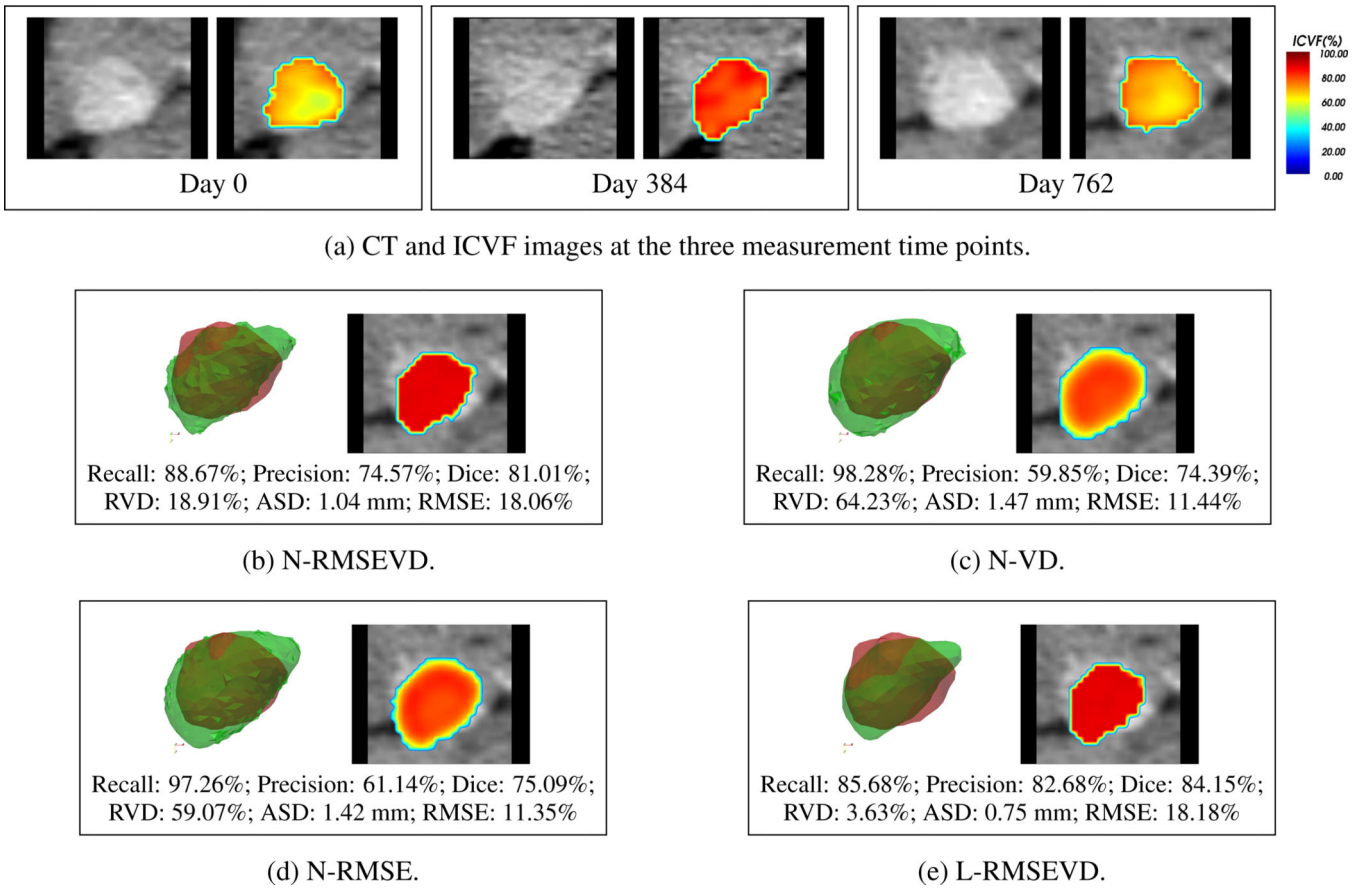

(a) CT and ICVF images at the three measurement time points.

(b) N-RMSEVD.

(c) N-VD.

(d) N-RMSE.

(e) L-RMSEVD.

Figure 9.

Clinical data. Patient 6. (a) CT and ICVF images at the three measurement time points. (b)–(e): prediction at the third time point, with the measured (red) and predicted (green) tumors superimposed.

Table 1

Sensitivity analysis. eFAST indices S (first-order) and S_T (total-order) of the model parameters corresponding to the average ICVF and the tumor volumes defined in (15).

	D_x	D_y	D_z	α	β	γ	λ_{tissue}	μ_{tissue}	λ_{tumor}	μ_{tumor}
S_{ICVF} (%)	1.61	1.75	1.90	38.04	30.69	0.08	0.04	0.02	0.03	0.04
$S_{T,ICVF}$ (%)	3.66	3.56	4.11	64.24	57.56	1.52	1.18	1.27	1.05	1.30
S_{Vol} (%)	0.11	0.11	0.05	34.63	28.98	0.05	0.04	0.03	0.07	0.03
$S_{T,Vol}$ (%)	1.97	2.25	1.07	69.18	64.47	1.30	0.62	0.56	0.76	0.44

Med Image Anal. Author manuscript; available in PMC 2016 October 01.

Table 2

Synthetic data. Estimated parameters, and the recall, precision, Dice coefficient, relative volume difference (RVD), average surface distance (ASD), and ICVF root-mean-squared error (RMSE). Format: mean±std [min,max].

(a) Estimated parameters corresponding to different ground-truth values of the SUV scaling parameter (α).

	D_x, D_y, D_z (mm^2/day, 10^{-3})			β (day^{-1}, 10^{-2})	γ (kPa)		α (mm^3/g/day)			
Ground truth	2.00	1.00	0.00	2.00	2.00	Ground truth	2.50	3.00	3.50	4.00
N-RMSEVD	1.71±0.37 [1.48,2.26]	0.89±0.19 [0.73,1.07]	0.03±0.03 [0.01,0.08]	2.08±0.83 [0.83,2.50]	1.98±0.03 [1.95,2.01]	N-RMSEVD	3.04	3.61	4.16	2.50
N-VD	1.74±1.10 [0.59,3.24]	0.83±0.58 [0.22,1.63]	0.13±0.12 [0.01,0.25]	2.45±0.10 [2.31,2.50]	2.35±0.72 [1.97,3.43]	N-VD	2.69	3.61	4.19	4.17
N-RMSE	1.50±0.65 [0.65,2.23]	0.70±0.31 [0.28,1.01]	0.14±0.22 [0.00,0.46]	2.08±0.83 [0.83,2.50]	2.41±1.06 [1.67,3.98]	N-RMSE	2.50	3.61	4.17	2.50
L-RMSEVD	1.64±0.38 [1.30,2.18]	0.86±0.17 [0.73,1.07]	0.04±0.05 [0.00,0.10]	2.08±0.83 [0.83,2.50]	4.47±0.20 [4.22,4.68]	L-RMSEVD	3.04	3.61	4.17	2.51

(b) Estimated parameters corresponding to different ground-truth values of the force scaling parameter (γ).

	D_x, D_y, D_z (mm^2/day, 10^{-3})			β (day^{-1}, 10^{-2})	α (mm^3/g/day)		γ (kPa)			
Ground truth	2.00	1.00	0.00	2.00	3.50	Ground truth	1.00	2.00	3.00	4.00
N-RMSEVD	1.62±0.04 [1.58,1.66]	0.74±0.01 [0.73,0.74]	0.03±0.02 [0.01,0.06]	2.49±0.01 [2.48,2.50]	4.13±0.02 [4.11,4.16]	N-RMSEVD	0.99	1.95	2.98	3.89
N-VD	1.52±0.05 [1.47,1.57]	0.73±0.04 [0.67,0.76]	0.01±0.01 [0.01,0.02]	2.50±0.01 [2.49,2.51]	4.20±0.02 [4.17,4.23]	N-VD	0.99	1.97	2.97	3.89
N-RMSE	1.54±0.05 [1.48,1.58]	0.74±0.02 [0.73,0.77]	0.01±0.00 [0.00,0.01]	2.50±0.01 [2.49,2.51]	4.17±0.01 [4.16,4.17]	N-RMSE	0.99	1.97	2.98	3.88
L-RMSEVD	1.89±0.50 [1.57,2.64]	0.92±0.25 [0.73,1.27]	0.08±0.13 [0.00,0.27]	2.51±0.03 [2.50,2.56]	4.16±0.03 [4.12,4.19]	L-RMSEVD	2.43	4.55	5.00	4.91

(c) Overall prediction performances.

	Recall (%)	Precision (%)	Dice (%)	RVD (%)	ASD (mm)	RMSE (%)
N-RMSEVD	98.43±0.81 [97.44,99.91]	99.67±0.25 [99.22,99.95]	99.04±0.36 [98.50,99.56]	1.44±0.57 [0.70,2.16]	0.04±0.02 [0.02,0.07]	0.93±0.24 [0.57,1.26]
N-VD	96.52±6.85 [81.02,99.58]	99.27±0.55 [98.38,99.68]	97.77±3.90 [88.94,99.54]	3.14±6.48 [0.24,17.81]	0.09±0.16 [0.02,0.45]	1.76±1.28 [0.97,4.55]
N-RMSE	93.65±12.15 [66.17,99.63]	99.76±0.29 [99.12,99.95]	96.21±7.32 [79.62,99.38]	6.26±12.16 [0.52,33.79]	0.12±0.21 [0.03,0.61]	2.89±4.96 [0.94,14.14]
L-RMSEVD	97.30±1.39 [94.40,98.90]	97.89±3.45 [90.18,99.78]	97.57±1.91 [93.80,99.13]	2.88±2.62 [0.48,8.35]	0.19±0.22 [0.08,0.67]	1.48±1.08 [0.71,3.80]

Table 3

Clinical data. Tumor information at the 1st, 2nd, and 3rd measurement time points.

Patient ID	1st–2nd		2nd–3rd		Size (cm^3, 3rd)	ICVF range (%, 3rd)	SUV max (g/ml, 1st)
	Days	growth (%)	Days	growth (%)			
1	384	34.60	804	33.36	2.26	[63.16, 84.12]	4.82
2	363	15.28	363	10.71	1.44	[64.50, 85.36]	6.23
3	378	18.91	372	7.54	0.36	[62.29, 83.82]	5.08
4	426	41.53	420	68.55	3.80	[63.36, 91.76]	26.87
5	372	7.44	360	12.46	6.27	[44.57, 83.83]	11.98
6	384	13.63	378	−3.86	1.57	[61.64, 84.53]	4.57
7	168	18.70	552	18.68	3.17	[56.03, 91.53]	7.76
8	363	16.87	525	34.66	0.30	[67.72, 88.19]	3.21

Med Image Anal. Author manuscript; available in PMC 2016 October 01.

Table 4

Clinical data. Estimated parameters, and the recall, precision, Dice coefficient, relative volume difference (RVD), average surface distance (ASD), and ICVF root-mean-squared error (RMSE). Format: mean±std [min,max].

(a) Estimated parameters and prediction performances before removing the outlier (Patient 7).

	D_x, D_y, D_z (mm^2/day, 10^{-3})			α (mm^3/g/day)	β (day^{-1}, 10^{-2})	γ (kPa)
N-RMSEVD	1.23±2.24 [0.01,6.73]	1.12±1.12 [0.00,3.52]	1.20±2.30 [0.13,6.85]	2.56±1.67 [0.56,5.00]	4.86±1.82 [1.67,8.33]	2.62±2.33 [0.15,7.22]
N-VD	2.39±2.42 [0.56,6.73]	3.53±2.67 [0.43,8.35]	3.88±4.00 [0.19,9.82]	2.92±1.72 [1.67,5.00]	5.28±1.95 [1.67,8.33]	5.10±2.88 [1.30,9.44]
N-RMSE	2.15±2.51 [0.56,6.87]	1.86±1.33 [0.19,3.85]	3.37±3.28 [0.93,9.82]	2.93±1.71 [1.67,5.00]	5.74±1.39 [5.00,8.33]	4.49±1.35 [1.87,6.11]
L-RMSEVD	0.60±0.29 [0.01,0.93]	0.74±0.76 [0.01,1.79]	1.17±1.54 [0.01,4.42]	2.92±1.72 [1.67,5.00]	5.03±1.72 [1.89,8.33]	4.79±3.31 [0.12,9.57]

	Recall (%)	Precision (%)	Dice (%)	RVD (%)	ASD (mm)	RMSE (%)
N-RMSEVD	84.53±6.91 [72.93,95.57]	85.79±8.18 [74.57,97.90]	84.59±1.67 [81.01,86.34]	14.21±8.43 [0.81,25.50]	0.76±0.22 [0.39,1.04]	12.58±3.20 [9.62,18.06]
N-VD	88.95±10.46 [68.01,99.46]	78.15±14.50 [58.69,99.02]	81.57±5.12 [73.82,86.78]	30.55±24.75 [0.81,69.47]	0.99±0.44 [0.41,1.72]	12.48±2.16 [9.62,16.32]
N-RMSE	83.76±12.28 [66.79,97.26]	84.05±12.88 [61.14,98.74]	82.29±3.97 [75.09,87.16]	25.63±16.86 [4.90,59.07]	0.86±0.33 [0.41,1.42]	12.01±1.88 [9.65,16.09]
L-RMSEVD	87.73±7.53 [79.10,100.00]	76.51±25.10 [17.40,96.52]	78.04±19.63 [29.65,87.94]	71.23±163.25 [1.16,474.58]	1.52±2.22 [0.32,6.97]	13.53±4.11 [9.73,21.03]

(b) Estimated parameters and prediction performances after removing the outlier (Patient 7).

	D_x, D_y, D_z (mm^2/day, 10^{-3})			α (mm^3/g/day)	β (day^{-1}, 10^{-2})	γ (kPa)
N-RMSEVD	1.27±2.42 [0.01,6.73]	1.20±1.19 [0.00,3.52]	0.39±0.30 [0.13,0.93]	2.69±1.76 [0.56,5.00]	4.84±1.97 [1.67,8.33]	2.75±2.48 [0.15,7.22]
N-VD	2.02±2.35 [0.56,6.73]	2.84±1.97 [0.43,5.00]	3.10±3.60 [0.19,9.82]	2.62±1.63 [1.67,5.00]	5.00±1.92 [1.67,8.33]	5.61±2.69 [1.30,9.44]
N-RMSE	1.48±1.76 [0.56,5.37]	1.58±1.14 [0.19,3.15]	2.81±3.12 [0.93,9.82]	3.11±1.77 [1.67,5.00]	5.85±1.46 [5.00,8.33]	4.62±1.40 [1.87,6.11]
L-RMSEVD	0.61±0.31 [0.01,0.93]	0.81±0.80 [0.01,1.79]	0.71±0.87 [0.01,2.37]	2.63±1.62 [1.67,5.00]	5.03±1.86 [1.89,8.33]	5.20±3.35 [0.12,9.57]

	Recall (%)	Precision (%)	Dice (%)	RVD (%)	ASD (mm)	RMSE (%)
N-RMSEVD	84.96±7.34 [72.93,95.57]	85.28±8.70 [74.57,97.90]	84.50±1.78 [81.01,86.34]	14.99±8.78 [0.81,25.50]	0.76±0.24 [0.39,1.04]	12.77±3.41 [9.62,18.06]
N-VD	87.45±10.33 [68.01,98.28]	80.93±13.16 [59.85,99.02]	82.67±4.37 [74.39,86.78]	24.99±20.64 [0.81,64.23]	0.89±0.36 [0.41,1.47]	12.27±2.24 [9.62,16.32]
N-RMSE	86.19±11.01 [70.02,97.26]	82.44±13.02 [61.14,98.74]	82.83±3.96 [75.09,87.16]	25.02±18.12 [4.90,59.07]	0.84±0.36 [0.41,1.42]	12.06±2.02 [9.65,16.09]
L-RMSEVD	85.97±6.11 [79.10,94.43]	84.95±8.36 [72.64,96.52]	84.95±1.86 [82.12,87.94]	13.60±10.16 [1.16,29.99]	0.74±0.27 [0.32,1.07]	12.46±3.01 [9.73,18.18]